3D Registration of mpMRI for Assessment of Prostate Cancer Focal Therapy

Clément Orczyk, MSc, MD[1], Andrew B. Rosenkrantz, MD, Artem Mikheev, MSc, Arnauld Villers, MD, PhD, Myriam Bernaudin, PhD, Samir S. Taneja, MD, Samuel Valable, PhD, Henry Rusinek, PhD

Rationale and Objectives: This study aimed to assess a novel method of three-dimensional (3D) co-registration of prostate magnetic resonance imaging (MRI) examinations performed before and after prostate cancer focal therapy.

Materials and Methods: We developed a software platform for automatic 3D deformable co-registration of prostate MRI at different time points and applied this method to 10 patients who underwent focal ablative therapy. MRI examinations were performed preoperatively, as well as 1 week and 6 months post treatment. Rigid registration served as reference for assessing co-registration accuracy and precision.

Results: Segmentation of preoperative and postoperative prostate revealed a significant postoperative volume decrease of the gland that averaged 6.49 cc ($P = .017$). Applying deformable transformation based on mutual information from 120 pairs of MRI slices, we refined by 2.9 mm (max. 6.25 mm) the alignment of the ablation zone, segmented from contrast-enhanced images on the 1-week post-operative examination, to the 6-month postoperative T2-weighted images. This represented a 500% improvement over the rigid approach ($P = .001$), corrected by volume. The dissimilarity by Dice index of the mapped ablation zone using deformable transformation vs rigid control was significantly ($P = .04$) higher at the ablation site than in the whole gland.

Conclusions: Our findings illustrate our method's ability to correct for deformation at the ablation site. The preliminary analysis suggests that deformable transformation computed from mutual information of preoperative and follow-up MRI is accurate in co-registration of MRI examinations performed before and after focal therapy. The ability to localize the previously ablated tissue in 3D space may improve targeting for image-guided follow-up biopsy within focal therapy protocols.

Key Words: Prostate cancer; focal therapy; longitudinal follow-up; MRI; image processing; three dimensional; biopsy; deformable registration.

INTRODUCTION

Contemporary methods of multiparametric magnetic resonance imaging (mpMRI) of the prostate have greatly improved the ability of radiologists and urologists to detect prostate cancer (1). mpMRI allows physicians to diagnose clinically significant cancer in its early stage, to

plan prostatectomy and radiation therapy, and to detect local recurrence.

Combined with the trend of earlier detection, noninvasive prostate cancer therapies are gaining interest. Focal therapies (FT) aim to combine oncologic benefit with preserved continence and erectile function. The use of this tissue-preservation approach is evolving, and FT are being applied to more aggressive disease than when initially proposed (2,3). Clinical FT trials depend on mpMRI for tumor localization, treatment planning, and posttreatment follow-up (4–7).

There is no consensus regarding optimal assessment of oncologic success of FT (3,5,8). Current criteria of successful FT involve negative histology at the treatment site. Different methods have been proposed to detect cancer recurrence after FT. Although invasive transrectal prostate biopsy or transperineal mapping biopsy are often performed, mpMRI-targeted biopsy has shown promising results (9,10). Such assessment by MRI requires an ability to delineate on imaging the ablation zone (AZ) that is characterized histologically by homogeneous coagulation necrosis (11,12). In addition, it has been suggested (7,13) that mpMRI underestimates the total tumor volume, requiring inclusion of some surrounding margin

within the AZ for a complete focal ablation. After treatment, dynamic contrast-enhanced (DCE) MRI delineates AZ as a devascularized, nonenhancing area (4). Within several weeks after treatment, the AZ shrinks, often leading to a changed configuration of the gland (8,14).

These novel therapeutic developments require a reliable and accurate software system for assessment of the changes in the prostate gland, including tissue necrosis, because of ablation. To be effective, such a system must depict how the viable tissue is reorganized around the AZ, thereby requiring a comparison of pretreatment and posttreatment images of the prostate. Development of image registration methods for this application is challenging. First, one must register longitudinal MRI, including different sequences, across different time points. Second, inherent in focal therapy, the tissue changes are inhomogeneous. Third, the variations in shape between the preoperative and the postoperative examinations are highly dependent on treatment delivery, location of the tumor, energy choice, and surrounding tissues. These factors make it difficult to use a normative atlas to facilitate registration.

Fei et al. (15) described a mutual information (MI)-based rigid-transform method to align a preoperative prostate T2-weighted (T2W) imaging sequence to an intraoperative sequence. Wu et al. (16) combined MI measure with low-order polynomial transformation to register spectroscopy with the prostate deformed by inflated intrarectal balloon. Using a finite elements method (FEM), Marami et al. (17) validated a registration approach between MRI acquired with an endorectal coil and the intraoperative MRI. Toth et al. (18) also used FEM to model the changes in prostate shape after laser ablation.

It has been previously demonstrated that the deformation of the gland after surgery is well captured by the affine transformation T that incorporates nonisotropic three-dimensional (3D) sheer and stretch factors (19). This technique was also found to accurately define a 3D target for focal therapy based on MRI findings (7). We have now implemented an image-based framework for accurate estimation of the affine transform from the pre-FT to the post-FT MRI. This study evaluates the method using longitudinal mpMRI acquired before and after modern interstitial laser (4) and photodynamic FT (20). This study aims to assess this novel method of 3D co-registration of prostate MRI examinations performed before and after prostate cancer focal therapy, to facilitate focal therapy follow-up.

MATERIALS AND METHODS

Patients

Ten male patients, aged 65 ± 6.4 years, diagnosed with localized prostate cancer at biopsy (median prostate-specific antigen 5.1 ng/mL, median Gleason Score 6) underwent FT. Five patients were treated by interstitial laser procedure within the MRI bore (4) and five by photodynamic therapy, included in an earlier publication (20). Local institutional review board approved this study.

Image Acquisition

All patients underwent a preoperative mpMRI, and two follow-up postoperative mpMRI (1 week and 6 months after treatment, Fig 1) using 3T Magnetom Trio system equipped with a pelvic phase array (Siemens Healthcare, Erlangen, Germany). Each examination used identical mpMRI protocol that included a T2W sequence, a diffusion-weighted sequence, and a DCE-MRI examination specified in detail below.

The anatomical T2W images through the pelvis were acquired using turbo spin echo sequence with the following parameters: repetition time = 4950 ms, echo time = 122 ms, axial orientation, 256×256 acquisition matrix, no interslice gap, 180×180 mm field of view, 3 mm slice thickness, and 3 signal averages.

Diffusion-weighted sequence was based on axial fat-suppressed single-shot echo-planar imaging with repetition time = 4100 ms; echo time = 86 ms; diffusion gradient b-values of 50 and 1000 s/mm²; slice thickness 3 mm; 100×100 matrix; 200×200 mm field of view, and 10 signal averages. Apparent diffusion coefficient maps were reconstructed in line.

DCE-MRI examination consisted of continuous acquisition of T1-weighted 3-mm-thick contiguous images (240×240 mm field of view; matrix 128×128) every 15 seconds after intravenous administration of 0.1 mmol/kg of gadopentetate dimeglumine (Magnevist; Bayer HealthCare Pharmaceuticals, Montville, NJ). The contrast agent was administered as an intravenous bolus via power injector (Spectris; Medrad, Warrendale, PA), followed by a 20-mL saline flush, both administered at a 3 mL/s injection rate.
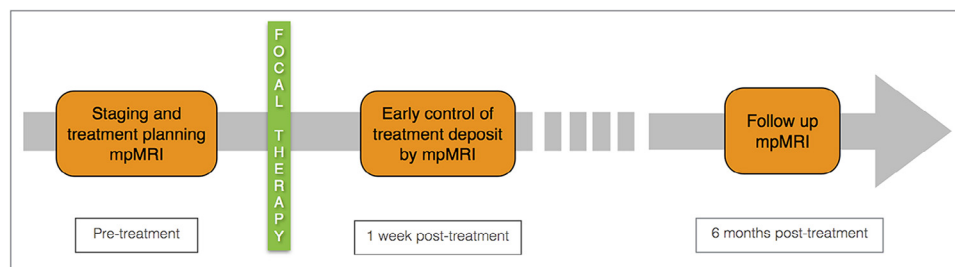

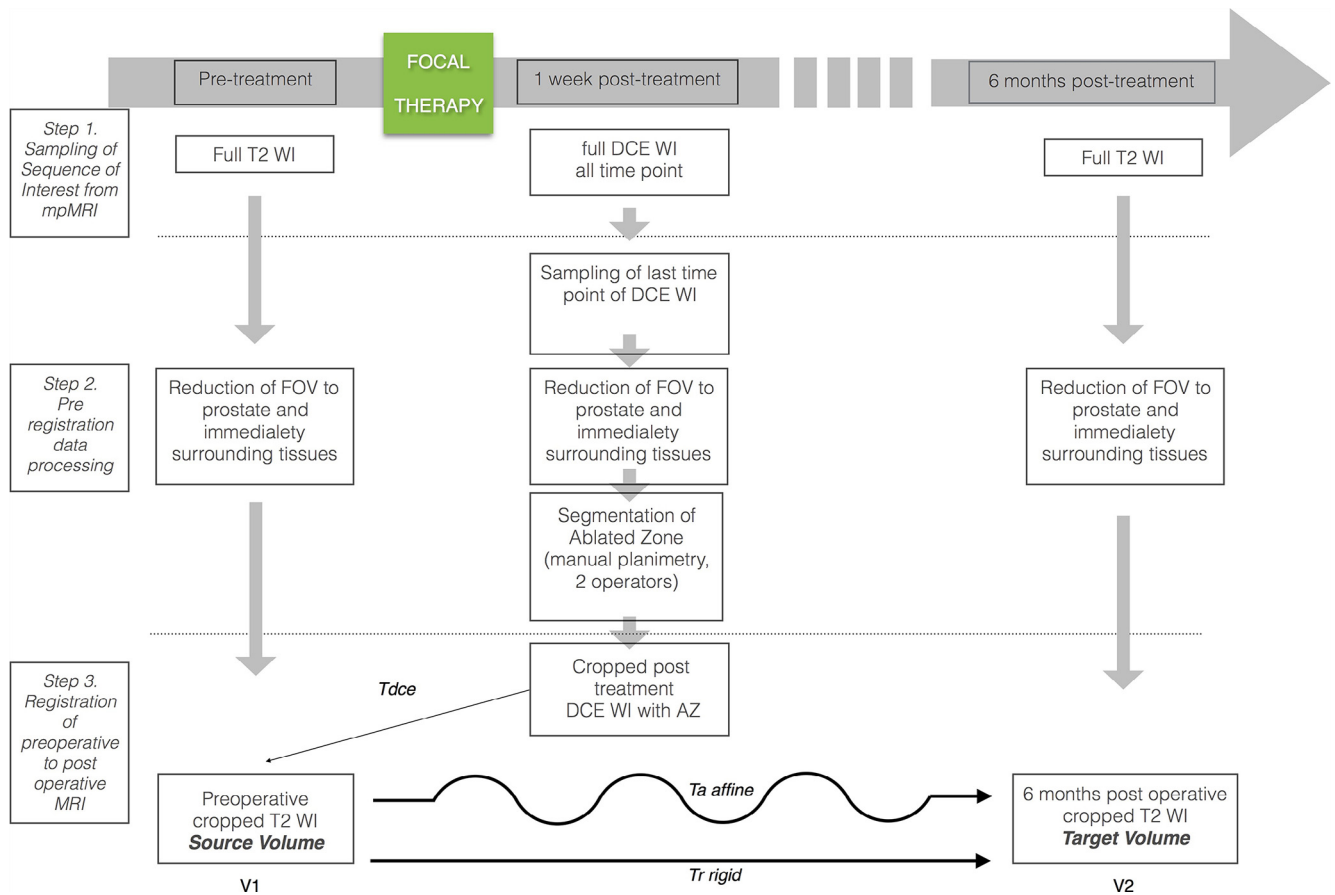**Figure 1.** Timeline of treatment and imaging examinations.

Figure 2. Image analysis workflow.

Image Analysis

Our image processing workflow (Fig 2) includes estimating 3D rigid body co-registration of mpMRI modalities within each examination, and image co-registration across examinations using nonrigid (affine) transform.
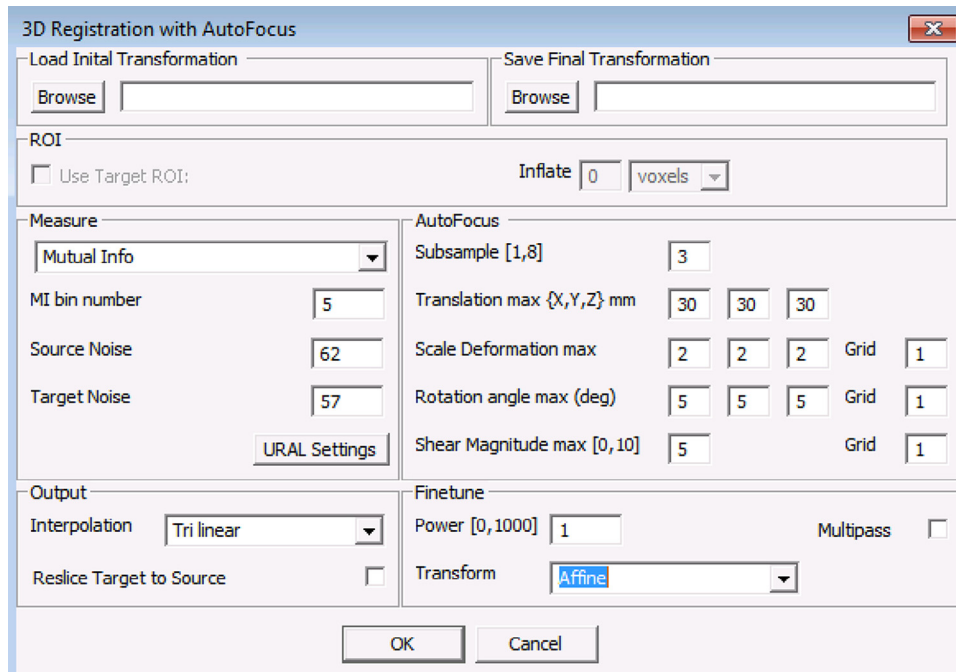
Co-registration Framework

The user interaction consists of a reduction of the field of view to the prostate gland and immediate surrounding tissues (step 2; Fig 2) that can be done in few seconds. A senior urologic surgeon performed this step.

There are several novel features of the system: (1) the parameters of the affine transform T are estimated only from prostate tissue, thus ignoring confounding signal from adjacent regions like the muscle, rectum, or the bladder; (2) the iterative voxel-similarity algorithm is supplemented by the multidimensional gridding of initial parameters. The goal is to make the estimate of T insensitive of the initial value and to avoid being trapped in a suboptimal local optimum; and (3) the software is designed to be used on multicore platforms.

Image co-registration consists of two tasks: determining the transformation T that relates points in the source image V_1 with the corresponding points in the target image V_2 and applying the transformation T to the source image, resulting in the co-registered volume $V_2' = T(V_1)$. Signal interpolation is

another necessary step. Our co-registration process is controlled using the dialog box shown in Fig 3. The optimization is done in two stages:

(1) "Autofocus" stage: exhaustive search over multiple initial approximations drawn from a discrete grid of parameters that define T (six parameters for rigid body, 12 parameters for affine transform). The most promising candidates (those having largest similarity measure) are passed to the second, fine-tune stage. The number of selected candidates is controlled by the "power" factor P. Large values of P may improve the accuracy of co-registration at the cost of longer processing time.

(2) "Fine-tune" stage: iterative search for a local maximum of the similarity measure (initialized at P settings from autofocus stage). We refine P most promising affine transforms using the parallelized implementation of the Nelder-Mead algorithm, a method for unconstrained optimization (21). The available measures include signal intensity differences (22), signal correlation (23), uniformity of ratio image (24,25), and MI and normalized MI (26–29). MI (30) was selected as the similarity metric because of its demonstrated robustness in multimodality registration, especially when applied within subject. MI has been used successfully in registration of prostate MRI (15,16).

Figure 3. The dialog box defines the registration process.

Although signal characteristics of untreated and treated tissue may be different, untreated portions of the gland constitute a vast majority of tissue volume (3).

Our framework allows the user to restrict the similarity measure to a predefined 3D region called "target." In this study, the target region was the prostate and immediately (approximately 5-mm margin) surrounding tissue (31). The idea is to focus the similarity on the organ of interest, whereas ignoring possible misalignment of background structures as well as confounding image (curves of bladder neck or anterior wall of rectum).

Estimating Transformations Within Examination and Across Examinations
The parameters for co-registering different MRI sequences within each examination were as follows: target region of interest (ROI) = yes, subsample = 3, autofocus grid = 10 mm, rotation = 10°, transform = rigid, measure = MI, interpolation = sinc. Co-registration of MRI sequences across examinations used the similar parameters except transform = affine, scale deformation = 2, and shear = 5. Here, a rigid method was explored as a control for affine, to assess the significance of deformation (stretching and sheering) induced by therapy, and to describe local changes that take place following FT.

For each patient and each examination, the resulting transformations were saved for later recall, to be applied to landmarks or subregion masks (ROI) placed within the source volume. This allowed visualization of AZ from the 1 week post-FT MRI superimposed over the prostate 6 months post FT.

The co-registration software was written in C++ using Microsoft Foundation Class and Intel Threading Building Blocks libraries. The program exploits parallel processing.

*Error Analysis and Segmentation of Prostate Gland and Ablation Zone*
To analyze registration error, two operators with experience in prostate anatomy manually segmented in consensus the different 3D masks (or ROIs): preoperative prostate, 6 months postoperative prostate, and AZ. ROIs excluded the seminal vesicles. The first two ROIs were traced on T2W images. Segmentation of the AZ, which was visualized in all 10 cases, was derived from the latest DCE time point from the 1-week post-FT MRI (Fig 4b). Ground truth segmentation was done in consensus by a radiologist who completed an abdominal radiology fellowship with more than 5 years' experience in interpretation of prostate mpMRI and a senior urologic surgeon with 3 years in practice. The geometrical transformations *T* estimated in the process of co-registration were applied to these 3D ROIs.

The ROIs served to assess the accuracy of rigid and non-rigid transformation models (Fig 5). It should be noted here that a future clinical or surgical use of the system does not require fine manual segmentation of the whole prostate.

We have measured the mismatch between transformed preop region and the region manually segmented at follow-up, the latter considered as the ground truth. Three types of error measures were evaluated:

(1) volume changes—although important, this measure is the least informative, because unlike the other two measures, it does not capture subtle shape changes.
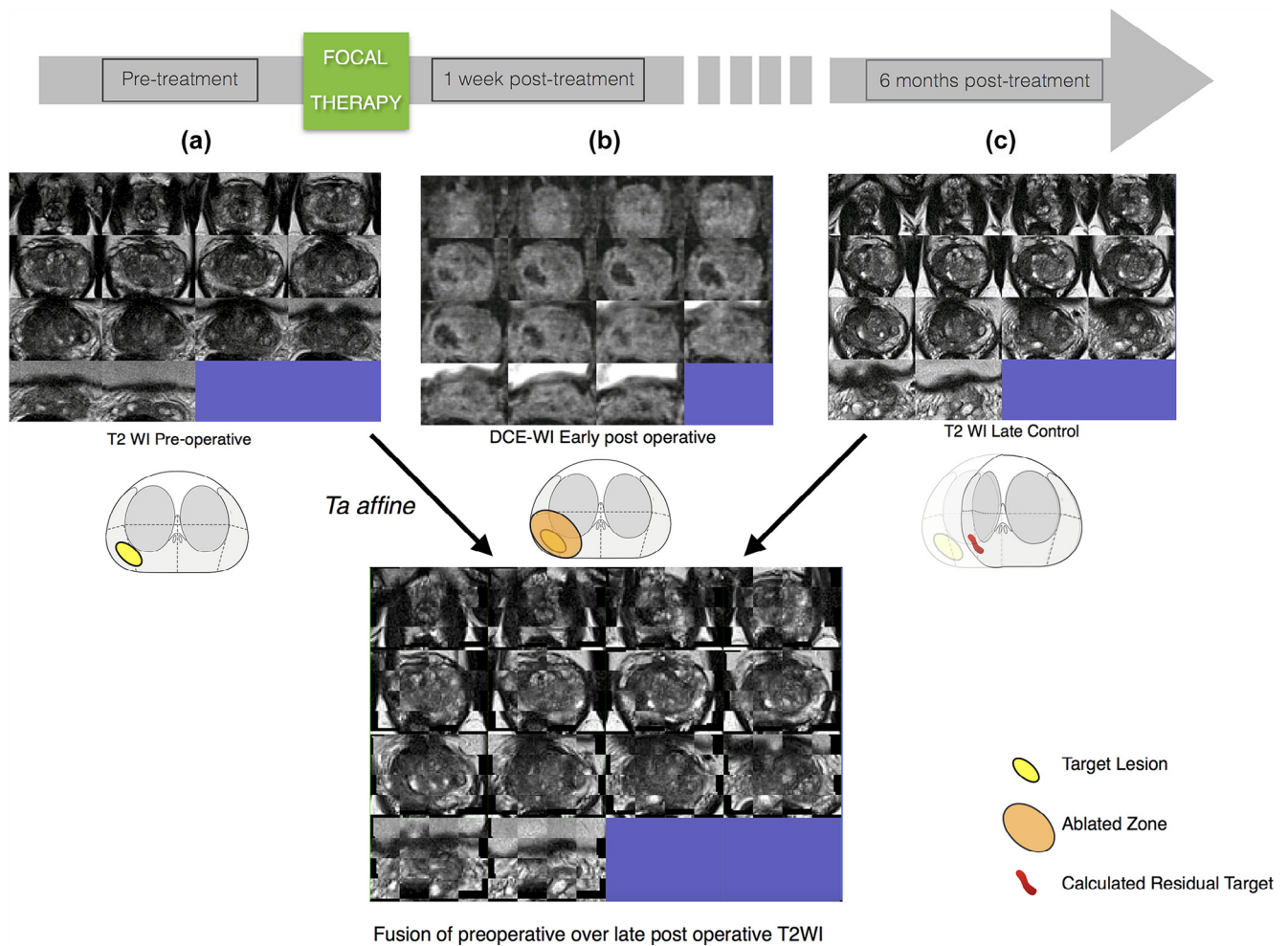
Figure 4. Illustrative case of affine registration between pretreatment **(a)** and posttreatment (photodynamic therapy) T2-weighted (T2W) volumes **(c)**. Panel **(b)** shows delayed dynamic contrast-enhanced (DCE) image of the treated area, with ablated gland shown as nonenhancing region. The bottom panel displays a postoperative T2W image overlayed with the corresponding preoperative image.

(2) the Hausdorff distance (HD), defined here as the maximum distance (in millimeters) between the structure boundaries (7). The HD was obtained for each slice composing an ROI. For each multislice ROI, the average of the maximum HD for each slice was calculated, resulting in an average maximum HD. The purpose is to have 3D information for each ROI.

(3) Dice index (19) was defined as the volume ratio $Di = 2 \times (A \cap B)/(A \cup B)$. The Dice index measures the normalized similarity between two different 3D masks ROIs based on their overlap.

The co-registration process aims to transfer the location of the effectively ablated zone AZ based on early postcontrast MRI to its residual location within the late control MRI. We further analyzed how the rigid Tr (V1) and nonrigid Ta (V1) transforms computed from MI measure for the entire gland (M = mask of whole gland) is able to align the AZ on V2 (late post-FT), as illustrated in Fig 2. This entails direct comparison of the derived target for post-FT follow-up between the compensated $AZ_{2'} = Ta(Tdce(AZ))$ and noncompensated

deformations $AZ_{2''} = Tr(Tdce(AZ))$. We compared Di $AZ_{2'}/AZ_{2''}$ to Di $M_{2'} = Ta(M)/M_{2''} = Tr(M)$ (Fig 5c). This compares the performances of the two algorithms at the location of the AZ to those for whole-gland mapping. Analogously, we compared the HD for the same ROIs, resulting in $AZ_{2'}$-$AZ_{2''}$ and $M_{2'}$-$M_{2''}$ (Fig 5c), normalized by volume.

These measures were compared using the paired t test or Wilcoxon signed rank test (for data that did not satisfy Shapiro-Wilk test of normality). A P value less than .05 was used to establish significance. All tests were done using R statistical software (version 3.0.2, Sep 2013, R foundation for Statistical Computing, Vienna, Austria).

RESULTS

Volumetric Analysis

There was a significant ~14% reduction in prostate volume (Table 1, Fig 6) between an average of 46.5 mL pre-FT and 40.0 mL post–FT ($P = .017$, paired t test, mean 6.50, 95%
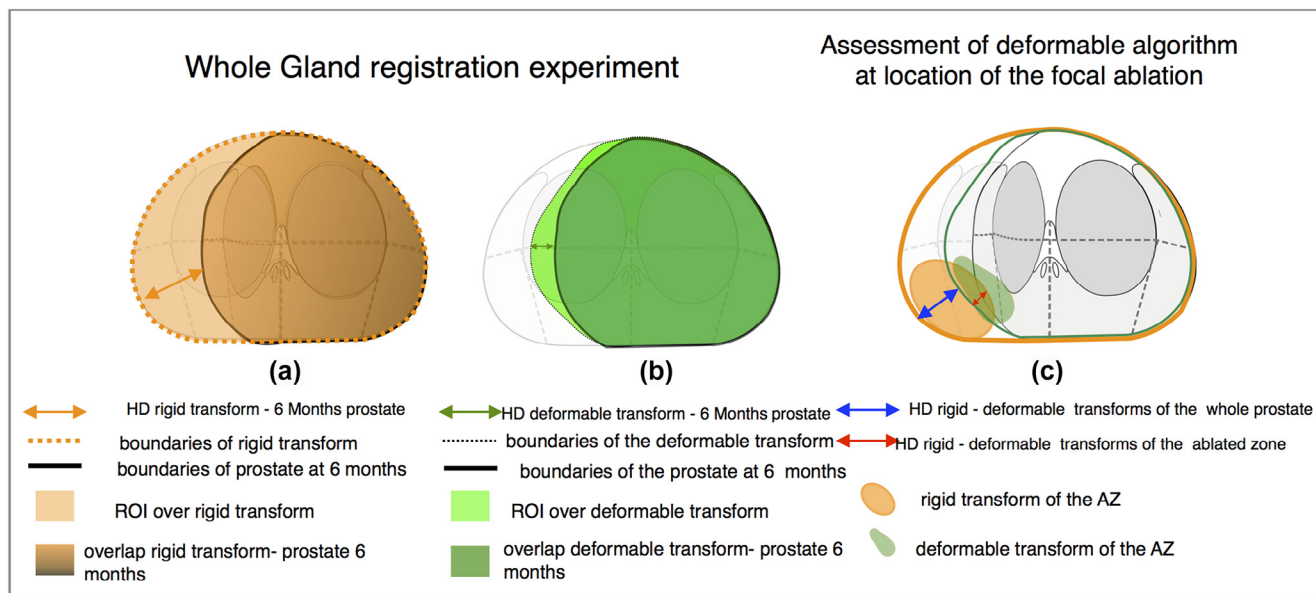
Figure 5. Schematic illustration of various measures assessed in the current study. **(a)** Analysis of errors in whole-gland definition for rigid transform model M_2 vs M_2''; **(b)** analysis of errors for affine transform model M_2 vs M_2'; and **(c)** analysis of errors in defining AZ (AZ_2–$AZ_{2''}$) vs (M_2'–M_2'').

TABLE 1. Distribution of Prostate Volumes Estimated from T2W Images Acquired Before and After Ablation (Late Control) and Distribution of Volume of Ablated Zone (AZ)

	Prostate Volume From T2W Images			Ablated Volume (cc) From DCE MRI
	Initial Volume (cc)	Postablation Volume (cc)	Difference D (cc)	
Median	51.64	46.73	6.70	7.88
Mean	46.49	39.99	6.50	13.82
SD	23.67	20.25	7.05	13.67
Min	8.42	6.80	−3.60	1.07
Max	87.16	65.52	21.64	37.35

DCE, dynamic contrast-enhanced; SD, standard deviation; T2W, T2-weighted.

confidence interval [CI] [1.46–11.54]). The volume of the AZ obtained by direct segmentation was significantly correlated (R = 0.738, P = .015) with the difference in prostate volume between the pre-FT and the post-FT examinations. However, the volume of AZ was on the average 13.8 mL, approximately double the difference D in pre-FT and post-FT volumes (Table 1) and statistically different from D (paired t test, T = −2.38, P = .04; mean diff. 7.33, 95% CI [0.38–14.27]).

The blue bars in Fig 6 illustrate the significant difference in volume between the rigid and the deformable transforms of the whole prostate over the late postoperative prostate at 6 months MRI, that is, M_2' vs M_2''.

Analysis of Image Co-registration

The 10 cases represented MRI volumes composed in total of 120 pair of slices for preoperative and late follow-up T2W imaging. In all cases, the MI algorithm converged successfully, and we were able to assess both nonrigid and rigid

transformations for co-registration of the pre-FT and post-FT images. The software architecture successfully exploited multicore processor parallelism and shown by high loading on a 12-core central processing unit system (Fig 7). A representative example is shown in Figure 4.

Table 2 compares of volume between the rigid M_2'', which serves as a control, and deformable M_2' transforms of the whole gland. The transforms of the pre-FT prostate to the post-FT prostate yielded a significantly lower volume (P = .041; mean difference 2.3, 95% CI [0.1132; 4.4868]) using nonrigid transformation compared to the rigid approach (Table 2). The difference of less than 1% of prostate volume after rigid transformation might be imputable to the interpolation errors, as rigid transformation conserves volume.

Table 3 lists the average values of Dice index and HD for the alignment of the whole gland described in Figure 5a and b. Although the alignment is better (smaller HD, larger overlap) for affine transform, the difference did not reach significance (P = .10 and .20). These comparisons suggest a trend for higher accuracy using the nonrigid transformation.
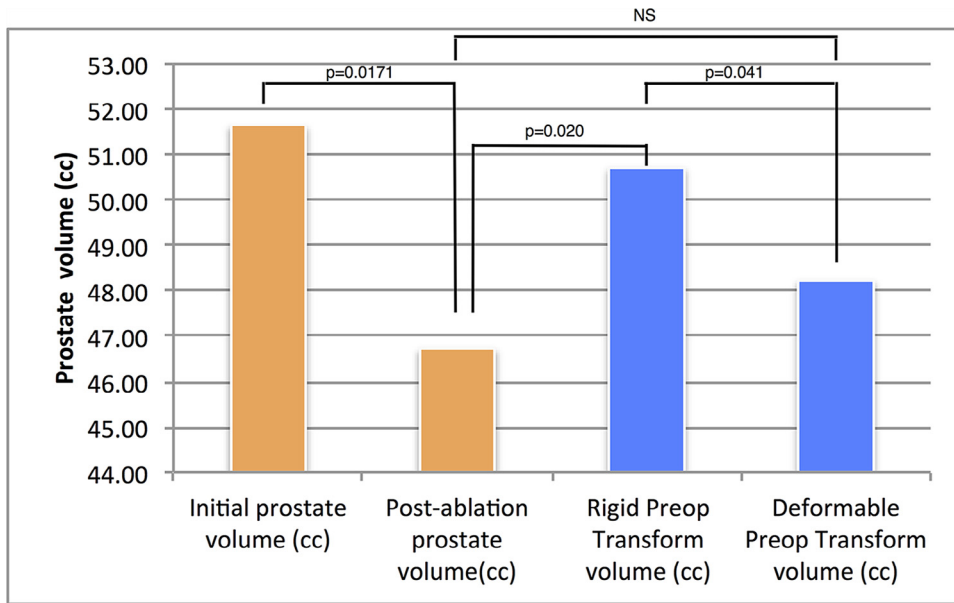
Figure 6. Comparison between median preoperative and 6-month postoperative volumes of the prostate (orange bars). Comparison between median volume generated with rigid and nonrigid transforms (blue bars) shows that nonrigid transformation compensates better for volume loss due to focal therapy. (Color version of figure is available online.)
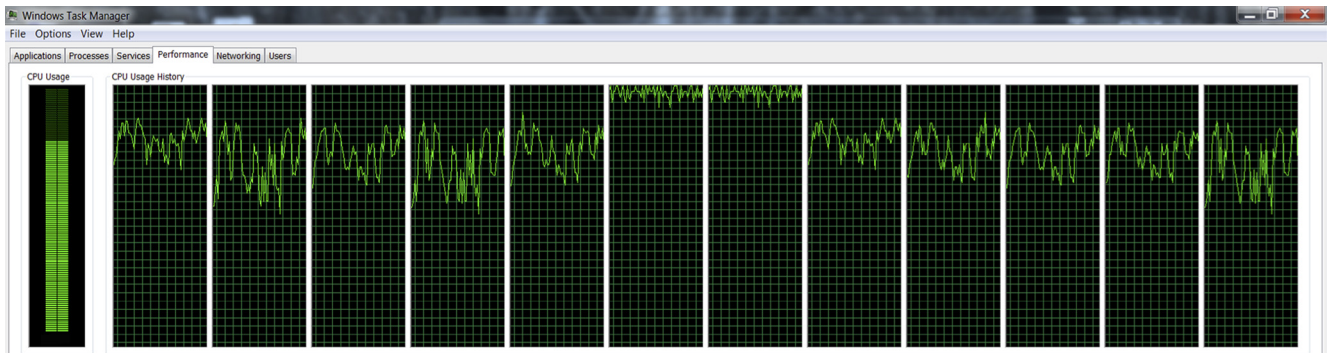
Figure 7. Demonstration of high central processing unit core usage on a 12-core computer achieved during registration.

TABLE 2. Comparison of Volumes Between Original T2WI and Their Transform Using Rigid and Deformable Methods

	Transformed Volumes	
	Rigid Preop Transform Volume (cc)	Deformable Preop Transform Volume (cc)
Median	50.71	48.22
Mean	45.41	43.23
SD	22.81	21.17
Min	7.99	7.17
Max	81.02	73.67

SD, standard deviation; T2W, T2-weighted image.

Analysis of AZ

When whole gland was taken into account, the nonrigid transformation Ta provided better description of AZ than did rigid transformation Tr (see Table 4), reaching 1.99 mm HD (or

0.72 mm/mL, $P = .0019$) and Di = 0.87 ($P = .046$) vs HD = 3.83 mm (or 0.15 mm mm/mL), and Di = 0.93.

Figure 8 illustrates the changes between pre- and post-treatment MRI at the ablated location, with a 3D reconstruction of the prostate.

DISCUSSION

The Role of Image Registration in Prostate Cancer Pathway

Image co-registration plays an increasingly important role in prostate cancer. It permits us to characterize MR signal and image texture of cancer tissue through histological validation (19,32,33). There is a great interest in developing ultrasound biopsy fused to MRI (34–37). Image registration will also play an important role in both planning and follow-up of FT. This entails accurate mapping of lesion mask derived from pretreatment mpMRI to the space of treatment and post-treatment images (7).

TABLE 3. Alignment Between Whole Gland Obtained by Mapping From Preoperative to Postoperative T2W Image and Whole Gland Traced Directly on Postoperative Image: Comparison Between Rigid and Affine Co-registrations

	Rigid Registration *Tr*	Affine Registration *Ta*
Hausdorff Distance (mm)		
Median	7.73	7.29
Mean	8.14	6.91
Max	9.46	9.98
Min	5.31	4.64
SD	1.45	1.60
P value	$P = .20$	
Dice Index		
Mean	0.82	0.84
Median	0.85	0.85
Max	0.91	0.92
Min	0.68	0.72
SD	0.08	0.06
P value	$P = .10$	

SD, standard deviation.

TABLE 4. Compensation of the Local Deformation by Affine Algorithm: Comparison Between Mapping Accuracy of the Location of the Ablated Zone and the Whole Gland, Referring to Measures Shown in Figure 5c

	Ta(AZ) vs *Tr* (AZ)	*Ta*(M) vs *Tr* (M)
Hausdorff Distance (mm)		
Median	1.99	3.83
Mean	2.99	3.84
Max	6.25	7.05
Min	1.10	1.10
SD	2.10	2.21
Normalized Hausdorff distance (mm/mL)		
Mean	0.72	0.15
Median	0.22	0.09
Max	1.09	0.55
Min	0.05	0.03
SD	0.57	0.17
P value	$P = .0019$	
Dice Index		
Mean	0.87	0.93
Median	0.87	0.92
Max	0.96	0.98
Min	0.59	0.88
SD	0.11	0.04
P value	$P = .046$	

SD, standard deviation.

The ability of contrast-enhanced imaging, either ultrasound or MRI, to visualize necrotic tissue permits initial assessment of FT (38). Several studies (3,5,8) converge by defining oncologic success of FT as negative biopsy at the treated area (prostate-specific antigen is not helpful for monitoring FT outcome (39)). Histological post-FT assessment depends on either random transrectal or transperineal approach (14,40). Transrectal option is prone to substantial sampling error and a high rate of false-negative results. Transperineal mapping option requires repeat general anesthesia (41). mpMRI offers the promise to guide post-FT biopsy and overcome these limitations (39,40,42,43). However, there are obvious concerns related to tissue displacement (42).

A critical step is to accurately locate AZ at follow-up biopsy to (1) evaluate the energy deposition within AZ, and (2) sample the surrounding tissue (tumor margin). The objective is to detect and manage treatment failure or cancer recurrence and possibly offer re-treatment. This task requires detecting low-volume cancer (39), and it requires exquisite precision. Ven et al. (44) estimated that, given a 0.3-mL target, a precision of 1.9 mm is necessary to correctly grade 95% of aggressive tumor component in peripheral zone. The report of the Standards of Reporting for MRI-targeted Biopsy Studies consortium concludes that defining the target for biopsy and being able to reliably sample such area remain fundamental problems (3). The challenge is intensified if a lesion is poorly demarcated on the post-FT images or if there are significant spatial deformations between pre- and post-FT images. To address this need, our study estimated the margin of error in AZ using affine transform and a novel co-registration framework. We chose rigid registration as a control.

Challenge for Image Registration

The current standard in radiologic in oncology is the Response Evaluation Criteria In Solid Tumors criteria, which unfortunately are subjective and do not involve image registration. There is very limited literature on longitudinal registration describing the deformation of the gland after local treatment (14,43). A recent report (18) aims to quantify changes of the gland after focal laser ablation using the FEM align pre- and postoperative T2W images. The study notes the importance of knowing biomechanical properties of the tissue, including surrounding bladder and rectum.

Posttreatment Volume Loss

We have observed a mean decrease in gland volume of 6.50 cc or 12.9%. This is significantly lower than the volume of the AZ, although the two measures were significantly correlated. Toth et al. (18) reported a similar decrease in gland volume at the same follow-up time delay in response to laser ablation. Volume shrinkage is likely caused by the process of *cicatrization* with fibrosis (45). If confirmed, accounting for volume change will be an important requirement of any longitudinal analysis software. Clearly, volume-preserving rigid
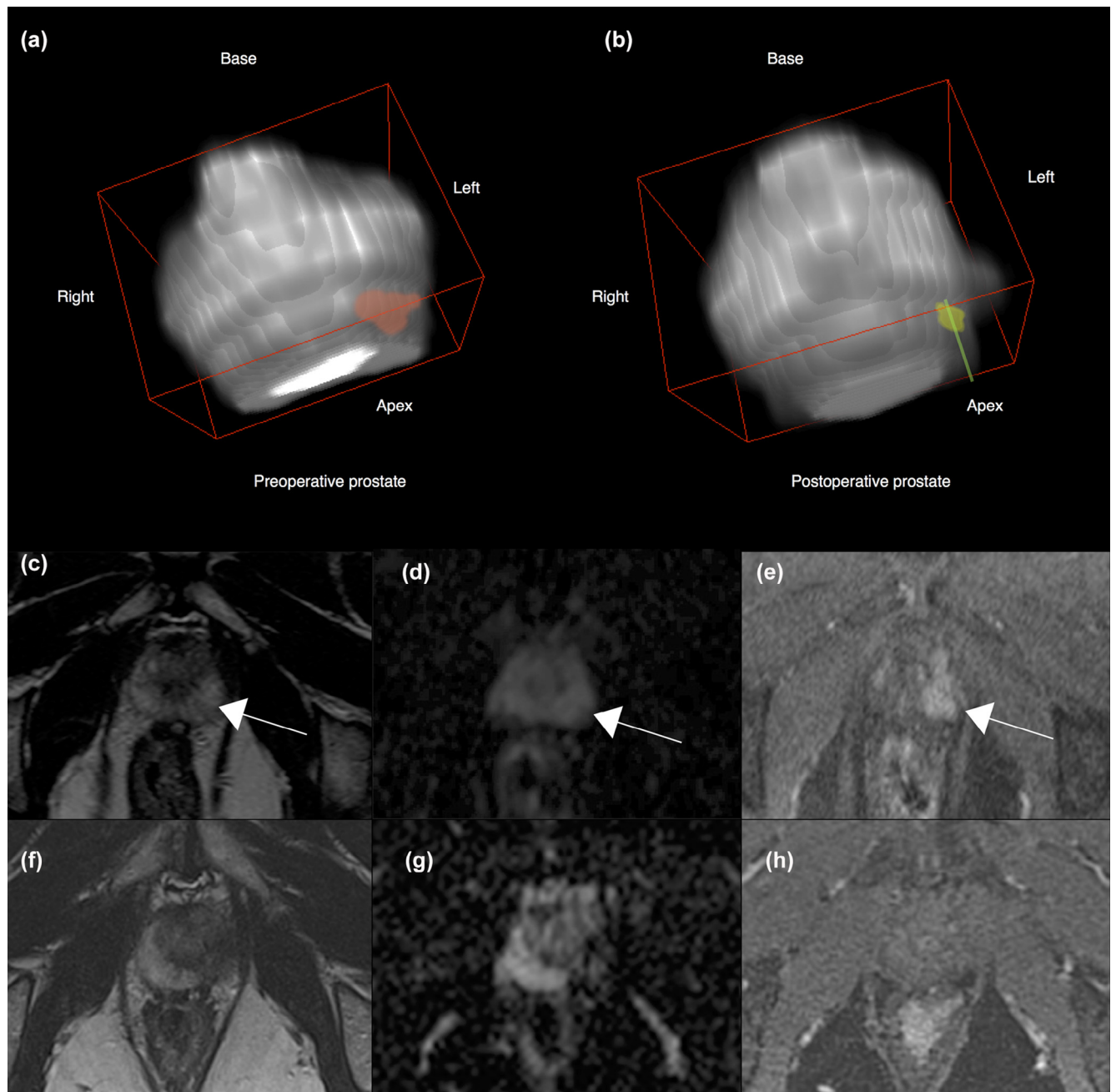
Figure 8. Postsurgical changes for a representative case involving dynamic phototherapy on the left lobe. **(a,b)** Three-dimensional (3D) rendering before and after treatment. Changes in shape and volume loss are observed in the left part of the gland. The pretreatment view shows in red the lesion 10 mm in axial diameter, Gleason 6 (3 + 3). The posttreatment view displays in yellow the location of the ablated zone. This yellow area needs to be sampled to rule out cancer at follow-up biopsy. The green line segment is the needle path for transperineal targeted biopsy. **(c)** Preoperative T2-weighted (T2W) image. **(d)** Preoperative apparent diffusion coefficient (ADC) map. **(e)** Preoperative dynamic contrast-enhanced (DCE) image through the cancer focus (white arrow). **(f)** Late postoperative T2W image. **(g)** Postoperative ADC map. **(h)** DCE image at the same level. Changes in shape and magnetic resonance imaging (MRI) signal are discernible at the site of ablation on the left side of the gland. (Color version of figure is available online.)

body co–registration is not capable of reflecting volume loss, whereas the affine transform appears to correctly represent the volume loss due to FT.

Co-registration Accuracy

Our image co-registration technique helps to assess FT and demonstrates that local treatment influences the deformation of the entire gland. We have observed the similarity of boundary changes at the gland (global) and the AZ (local) level. Both Dice index and HD show the effect of nonrigid algorithm at AZ. The change in mean HD of 2.9 mm (maximum ~6 mm) between rigid and a nonrigid mapped AZ indicates the advantage of the deformable model to define an area of interest. This observation is important because it implies that currently

available systems that ignore shrinkage may leave unsampled residual tissue and fail to detect residual or recurrent disease.

We have also demonstrated that changes in AZ are well modeled by the affine transform. Normalized HD resulting from affine compensation was 0.75 mm/cc for the AZ, which is almost five times better than 0.15 mm/cc for the whole gland. The lower Dice index at the AZ location (0.88) in this experiment compared to the whole gland (0.93) indicates the higher dissimilarity of the rigid and nonrigid transforms at this very zone of interest. These data indicate that the residual tissue at the former AZ location is more accurately mapped in the post–FT MRI using the nonrigid approach than without such compensation. This important finding shows the ability to successfully model tissue changes at the location of cancer that can be visualized on baseline mpMRI. Intensity changes at the location of the ablation were also reported by Toth et al. (18).

We attribute good performance of longitudinal co-registration (all the attempted registrations were successful) to the use of discrete parameter gridding, introduced to avoid being trapped in local maxima. Moreover, our method computes the similarity measures from prostate alone. The reduced field of view decreases the computational effort and is not in-fluenced by tissue motion outside the prostate. MI has been used in several applications for prostate registration like histology-MRI correlation (19,46) and intraprocedural registration of MRI for focal ablation (15,47). The computation of the joint histogram for MI, as a fully image-based method, seems to enable the registration. Longitudinal registration of medical imaging is still an area of active research (48). The implementation of multicore parallelism enables one to complete this complex task on standard desktop computer in a few minutes.

Limitations

We have evaluated the registration technique using volumetric and linear metrics (Dice index and HD) rather than using more conventional landmark approach. Clearly identifiable landmarks are hard to detect on postoperative images. Assessment of the method in a larger cohort would be useful for validation of those initial findings.

Our co-registration procedure includes manual steps in which the operator delineates the prostate gland and surrounding (approximately 5 mm) tissue. In a future study, we plan to investigate (1) the relationship between the size of the mask
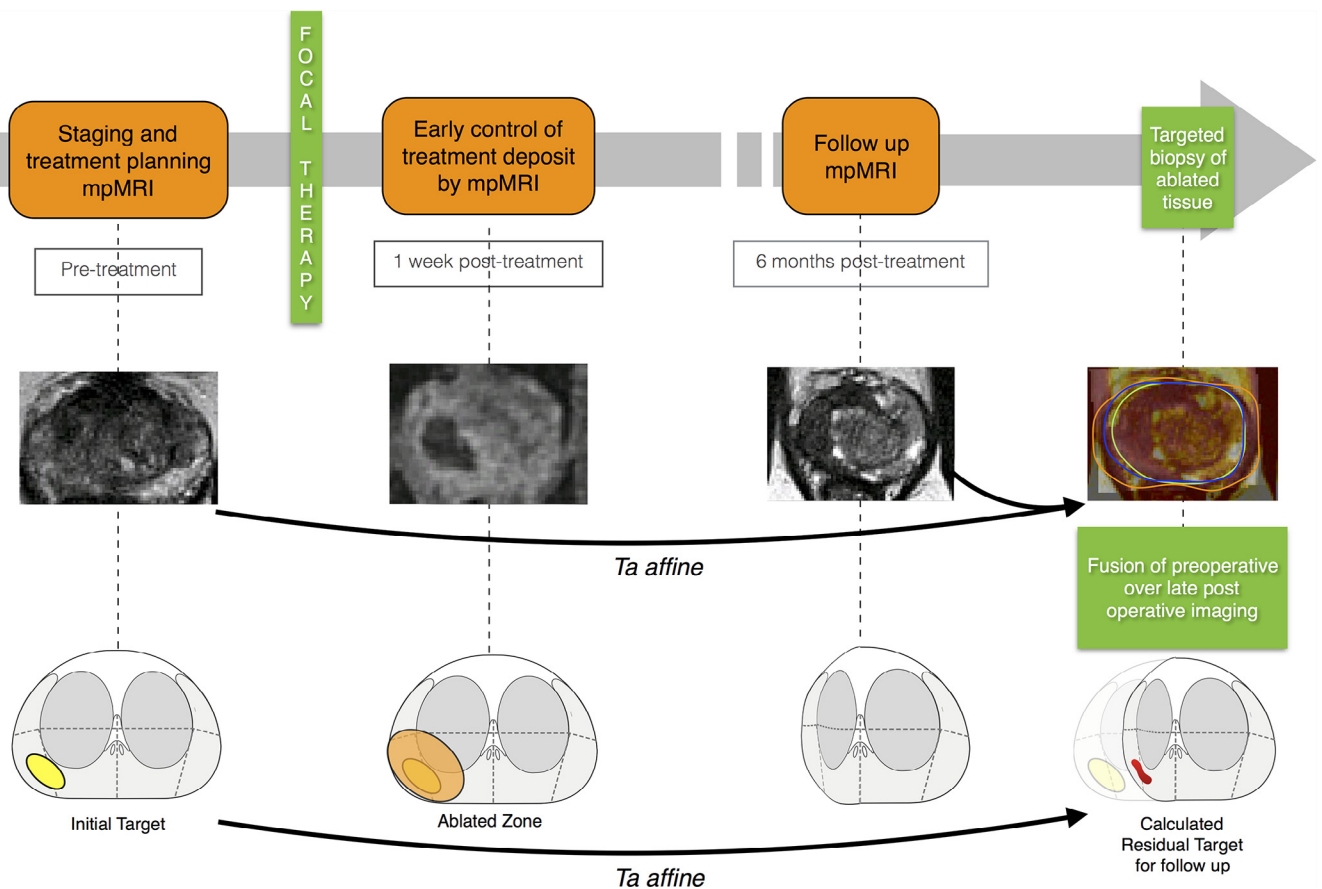
Figure 9. Graphical summary of implementation of three-dimensional (3D) registration of multiparametric magnetic resonance imaging (mpMRI) into focal therapy of prostate cancer pathway. Overlays of the prostate segmentation are presented on the extreme right MRI image with the green line as the postablation segmentation, the blue the preoperative registered prostate using the nonrigid transformation, and the orange using the rigid registration. (Color version of figure is available online.)

and the registration accuracy, and (2) interobserver variability of the method.

Clinical Implications

This work suggests that longitudinal image transformation may guide the location of targeted biopsy after FT. The shrinkage of AZ can be modeled before follow-up biopsy and incorporated in an ultrasound-guided sampling system (49). A recent study evocated the benefit of a transrectal ultrasonography-MRI fusion platform that corrects for deformation on ultrasound because of the probe insertion, as compared to "cognitive registration" (10). Such implementation could also be used in MR bore biopsy procedure (50). Using longitudinal co-registration, one could consistently revisit the same gland location (51), without limitations of implantable or imageable pellets proposed recently by Ghai and Trachtenberg (52). Recently, Natarajan et al. (53) raised the question of assessment of treatment margin in their report of a phase 1 trial about focal therapy using in-bore laser ablation with a transrectal approach. Our method may assist to discriminate infield-outfield recurrence after focal therapy. Figure 9 summarizes the potential clinical implementation of our findings in focal therapy pathway and follow-up.

Toth and associates (18) provide preliminary validation of a competing framework based on FEM and requiring modeling the elastic effects of the bladder and the rectum. A direct comparison between FEM and purely image-based framework would be of interest. Although further work is needed to validate software for accurate and safe focal therapy procedures, our preliminary experience suggests the clinical utility of affine algorithms for mapping mpMRI findings between pre- and post-FT scans. Our workflow could be also extended to transformation models that involve higher degree of freedom. The longitudinal co-registration technique could also be applied to other image-guided procedures like liver ablation (54) or focal kidney-sparing cancer therapy (55).

In summary, we have proposed a novel co-registration framework that has potential to provide image-guided target for post-FT biopsy. The affine algorithm can compensate and correct the deformation of an ablated zone and reach the needed accuracy of several millimeters. The technique offers the possibility to revisit cancer location that was targeted, and to plan follow-up biopsy, facilitating accurate and safe follow-up of focal therapy of prostate cancer.

REFERENCES

1. Dickinson L, Ahmed HU, Allen C, et al. Magnetic resonance imaging for the detection, localisation, and characterisation of prostate cancer: recommendations from a European consensus meeting. Eur Urol 2011; 59:477–494.
2. Orczyk C, Emberton M, Ahmed HU. What tumours should we treat with focal therapy based on risk category, grade, size and location? Curr Opin Urol 2015; 25:212–219.
3. Donaldson IA, Alonzi R, Barratt D, et al. Focal therapy: patients, interventions, and outcomes—a report from a consensus meeting. Eur Urol 2015; 67:771–777.
4. Oto A, Sethi I, Karczmar G, et al. MR imaging-guided focal laser ablation for prostate cancer: phase I trial. Radiology 2013; 267:932–940.
5. van den Bos W, Muller BG, Ahmed H, et al. Focal therapy in prostate cancer: international multidisciplinary consensus on trial design. Eur Urol 2014; 65:1078–1083.
6. Le Nobin J, Orczyk C, Deng F-M, et al. Prostate tumour volumes: evaluation of the agreement between magnetic resonance imaging and histology using novel co-registration software: prostate tumour volume: co-registration between MRI and pathology. BJU Int 2014; 114(6b):E105–E112.
7. Le Nobin J, Rosenkrantz AB, Villers A, et al. Image guided focal therapy for magnetic resonance imaging visible prostate cancer: defining a 3-dimensional treatment margin based on magnetic resonance imaging histology co-registration analysis. J Urol 2015; 194:364–370.
8. Muller BG, van den Bos W, Brausi M, et al. Follow-up modalities in focal therapy for prostate cancer: results from a Delphi consensus project. World J Urol 2015; 33:1503–1509. Available at: http://link.springer.com/10.1007/s00345-014-1475-2. Accessed February 9, 2015.
9. Rosenkrantz AB, Taneja SS. Targeted prostate biopsy: opportunities and challenges in the era of multiparametric prostate magnetic resonance imaging. J Urol 2012; 188:1072–1073.
10. Wysock JS, Rosenkrantz AB, Huang WC, et al. A prospective, blinded comparison of magnetic resonance (MR) imaging-ultrasound fusion and visual estimation in the performance of MR-targeted prostate biopsy: the PROFUS trial. Eur Urol 2014; 66:343–351.
11. Lindner U, Lawrentschuk N, Weersink RA, et al. Focal laser ablation for prostate cancer followed by radical prostatectomy: validation of focal therapy and imaging accuracy. Eur Urol 2010; 57:1111–1114.
12. Huang Z, Haider MA, Kraft S, et al. Magnetic resonance imaging correlated with the histopathological effect of Pd-bacteriopheophorbide (Tookad) photodynamic therapy on the normal canine prostate gland. Lasers Surg Med 2006; 38:672–681.
13. Bratan F, Melodelima C, Souchon R, et al. How accurate is multiparametric MR imaging in evaluation of prostate cancer volume? Radiology 2014; 140524.
14. Rouvière O, Gelet A, Crouzet S, et al. Prostate focused ultrasound focal therapy—imaging for the future. Nat Rev Clin Oncol 2012; 9:721–727.
15. Fei B, Wheaton A, Lee Z, et al. Automatic MR volume registration and its evaluation for the pelvis and prostate. Phys Med Biol 2002; 47:823–838.
16. Wu X, Dibiase SJ, Gullapalli R, et al. Deformable image registration for the use of magnetic resonance spectroscopy in prostate treatment planning. Int J Radiat Oncol Biol Phys 2004; 58:1577–1583.
17. Marami B, Sirouspour S, Ghoul S, et al. Elastic registration of prostate MR images based on estimation of deformation states. Med Image Anal 2015; 21:87–103.
18. Toth R, Sperling D, Madabhushi A. Quantifying post-laser ablation prostate therapy changes on MRI via a domain-specific biomechanical model: preliminary findings. PLoS ONE 2016; 11:e0150016.
19. Orczyk C, Rusinek H, Rosenkrantz AB, et al. Preliminary experience with a novel method of three-dimensional co-registration of prostate cancer digital histology and in vivo multiparametric MRI. Clin Radiol 2013; 68:e652–e658.
20. Taneja SS, Bennett J, Coleman J, et al. Final results of a phase I/II multicenter trial of WST11 (TOOKAD® Soluble) vascular-targeted photodynamic therapy (VTP) for hemiablation of the prostate in men with unilateral low risk prostate cancer conducted in the United States. J Urol 2016; 196:1096–1104.
21. Lagarias J, Reeds J, Wright M, et al. Convergence properties of the Nelder–Mead simplex method in low dimensions. SIAM J Optim 1998; 9:112–147.
22. Hajnal JV, Saeed N, Oatridge A, et al. Detection of subtle brain changes using subvoxel registration and subtraction of serial MR images. J Comput Assist Tomogr 1995; 19:677–691.
23. Lemieux L, Wieshmann UC, Moran NF, et al. The detection and significance of subtle changes in mixed-signal brain lesions by serial MRI scan matching and spatial normalization. Med Image Anal 1998; 2:227–242.
24. Woods RP, Grafton ST, Holmes CJ, et al. Automated image registration: I. General methods and intrasubject, intramodality validation. J Comput Assist Tomogr 1998; 22:139–152.
25. Woods RP, Grafton ST, Watson JD, et al. Automated image registration: II. Intersubject validation of linear and nonlinear models. J Comput Assist Tomogr 1998; 22:153–165.

26. Collignon A, Maes F, Delaere D, et al. Automated multi-modality image registration based on information theory. In: Bizais. 1995.
27. Maes F, Collignon A, Vandermeulen D, et al. Multimodality image registration by maximization of mutual information. IEEE Trans Med Imaging 1997; 16:187–198.
28. Viola P, Wells WM. Alignment by maximization of mutual information. In: Fifth international conference on computer vision, 1995. Proceedings. 1995; 16–23.
29. Wells WM, 3rd, Viola P, Atsumi H, et al. Multi-modal volume registration by maximization of mutual information. Med Image Anal 1996; 1:35–51.
30. James AP, Dasarathy BV. Medical image fusion: a survey of the state of the art. Inf Fusion 2014; 19:4–19.
31. Park B, Mikheev A, Zaim Wadghiri Y, et al. Optimal target VOI size for accurate 4D coregistration of DCE-MRI. Vol. 9788. 2016. Available at: http://dx.doi.org/10.1117/12.2214675. Accessed April 19, 2016. 97881P–97881P–8.
32. Gibson E, Crukley C, Gaed M, et al. Registration of prostate histology images to ex vivo MR images via strand-shaped fiducials. J Magn Reson Imaging 2012; 36:1402–1412.
33. Patel P, Chappelow J, Tomaszewski J, et al. Spatially weighted mutual information (SWMI) for registration of digitally reconstructed ex vivo whole mount histology and in vivo prostate MRI. In: IEEE. 2011; 6269–6272. Available at: http://ieeexplore.ieee.org.ezproxy.med.nyu.edu/xpls/abs_all.jsp?arnumber=6091547&tag=1. Accessed March 2, 2012.
34. Hawkes DJ, Barratt D, Blackall JM, et al. Tissue deformation and shape models in image-guided interventions: a discussion paper. Med Image Anal 2005; 9:163–175.
35. Hu Y, Carter T, Ahmed H, et al. Modelling prostate motion for data fusion during image-guided interventions. IEEE Trans Med Imaging 2011; 30:1887–1900. Available at: http://www.ncbi.nlm.nih.gov/pubmed/21632296. Accessed July 12, 2011.
36. Hu Y, Morgan D, Ahmed HU, et al. A statistical motion model based on biomechanical simulations for data fusion during image-guided prostate interventions. Med Image Comput Comput Assist Interv 2008; 11(Pt 1):737–744.
37. Mitra J, Kato Z, Martí R, et al. A spline-based non-linear diffeomorphism for multimodal prostate registration. Med Image Anal 2012; 16:1259–1279.
38. Rouvière O, Glas L, Girouin N, et al. Prostate cancer ablation with transrectal high-intensity focused ultrasound: assessment of tissue destruction with contrast-enhanced US. Radiology 2011; 259:583–591.
39. Barret E, Harvey-Bryan K-A, Sanchez-Salas R, et al. How to diagnose and treat focal therapy failure and recurrence? Curr Opin Urol 2014; 24:241–246.
40. Muller BG, van den Bos W, Pinto PA, et al. Imaging modalities in focal therapy: patient selection, treatment guidance, and follow-up. Curr Opin Urol 2014; 24:218–224.
41. Muller BG, Fütterer JJ, Gupta RT, et al. The role of magnetic resonance imaging (MRI) in focal therapy for prostate cancer: recommendations from a consensus panel: role of MRI in focal therapy for prostate cancer. BJU Int 2014; 113:218–227.
42. De Visschere PJ, De Meerleer GO, Fütterer JJ, et al. Role of MRI in follow-up after focal therapy for prostate carcinoma. AJR Am J Roentgenol 2010; 194:1427–1433.
43. Del Vescovo R, Pisanti F, Russo V, et al. Dynamic contrast-enhanced MR evaluation of prostate cancer before and after endorectal high-intensity focused ultrasound. Radiol Med 2013; 118:851–862.
44. Ven WJM, Hulsbergen-van de Kaa CA, Hambrock T, et al. Simulated required accuracy of image registration tools for targeting high-grade cancer components with prostate biopsies. Eur Radiol 2012; 23:1401–1407.
45. Shah TT, Kasivisvanathan V, Jameson C, et al. Histological outcomes after focal high-intensity focused ultrasound and cryotherapy. World J Urol 2015; 1–10.
46. Chappelow J, Madabhushi A. Multi-attribute combined mutual information (MACMI): an image registration framework for leveraging multiple data channels. In: 2010 IEEE international symposium on biomedical imaging: from nano to macro. IEEE, 2010; 376–379.
47. Fei B, Lee Z, Boll DT, et al. Image registration and fusion for interventional MRI guided thermal ablation of the prostate cancer. In: Medical image computing and computer-assisted intervention—MICCAI 2003. Berlin, Heidelberg: Springer, 2003; 364–372. Available at: https://link.springer.com/chapter/10.1007/978-3-540-39903-2_45. Accessed March 12, 2017.
48. Gerig G, Fishbaugh J, Sadeghi N. Longitudinal modeling of appearance and shape and its potential for clinical use. Med Image Anal 2016; 33:114–121.
49. Mozer P, Baumann M, Chevreau G, et al. Mapping of transrectal ultrasonographic prostate biopsies: quality control and learning curve assessment by image processing. J Ultrasound Med 2009; 28:455–460.
50. Engelhard K, Kühn R, Osten A, et al. Impact of magnetic resonance imaging-guided prostate biopsy in the supine position on the detection of significant prostate cancer in an inhomogeneous patient cohort. Scand J Urol 2016; 50:110–115.
51. Ukimura O, Gross ME, de Castro Abreu AL, et al. A novel technique using three-dimensionally documented biopsy mapping allows precise re-visiting of prostate cancer foci with serial surveillance of cell cycle progression gene panel: re-visiting biopsy from known prostate cancer. Prostate 2015; 75:863–871.
52. Ghai S, Trachtenberg J. Prostate cancer: a consensus on trial design for focal therapy. Nat Rev Urol 2014; 11:190–192.
53. Natarajan S, Raman S, Priester AM, et al. Focal laser ablation of prostate cancer: phase I clinical trial. J Urol 2016; 196:68–75.
54. Lencioni R, de Baere T, Martin RC, et al. Image-guided ablation of malignant liver tumors: recommendations for clinical validation of novel thermal and non-thermal technologies—a western perspective. Liver Cancer 2015; 4:208–214.
55. Singla N, Gahan J. New technologies in tumor ablation. Curr Opin Urol 2016; 26:248–253.